CHEMISTRY OF MATERIALS

pubs.acs.org/cm

Article

Skin-Like Near-Infrared II Photodetector with High Performance for Optical Communication, Imaging, and Proximity Sensing

Yu Zhu, Chen Geng, Lianghao Hu, Lin Liu, Yangzhi Zhu, Yao Yao, Chenxi Li, Yanfeng Ma, Guanghui Li,* and Yongsheng Chen*

Cite This: https://doi.org/10.1021/acs.chemmater.2c03701

Read Online

ACCESS | Metrics & More | Article Recommendations | Supporting Information

ABSTRACT: Skin-like second-near-infrared (NIR-II) photodetectors are key requirements for a flexible photodetection system that can be seamlessly integrated with three-dimensional geometries to accurately distinguish and acquire real-time various information. However, such devices exhibiting simultaneously high photosensitivity, fast photoresponse, and excellent flexibility still remain elusive. Here, we design and fabricate such skin-like NIR-II photodetectors and arrays with a simple bilayer configuration by combining a highly conducting MXene ($Ti_3C_2T_x$) and photosensitive lead sulfide quantum dots (PbS QDs), where highly promoted photocarrier separation at the interface of bilayers and efficient transport across the spatially separated layers could be achieved. Moreover, the bilayer architecture together with the strong interface bonding between the MXene and PbS QDs ensure a high-quality interface, leading to simultaneously improved optoelectronic performance and mechanical stability. Thus, the resulting device exhibits a high responsivity (1000 mA W^{-1}), a fast photoresponse (30 ms), and excellent mechanical stability (>95% performance retention after 500 cycle bending), which renders this skin-like NIR-II photodetector highly suitable for fabricating various practical and high-performance flexible wireless photodetection systems for optical communication, NIR-II imaging, and proximity sensing in different environments. We anticipate that this simple yet high-performance skin-like MXene/PbS QDs-based photodetector would hold great potential in the applications of next-generation flexible optoelectronics.

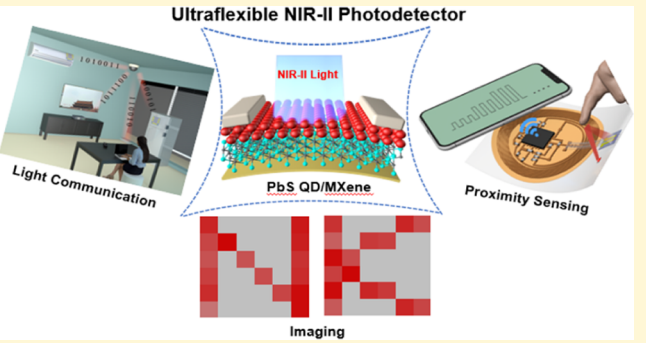

1. INTRODUCTION

Flexible second-near-infrared (NIR-II) photodetectors and arrays, especially skin-like photodetectors, that can seamlessly integrate with a curved surface have considerable advantages in terms of optical communication, NIR-II imaging, light detection and ranging (LiDAR) sensing, and biological health monitoring.[1−7] Specifically, their capability of laminating on three-dimensional (3D) objects makes them a key element in complex environmental conditions to distinguish and acquire extensive information.[8−10] Indeed, tremendous efforts have been made to improve the optoelectronic performance and mechanical stability of NIR-II photodetectors. However, most of these devices exhibit either poor sensitivity or slow photoresponse.[2,3,11−15] The fundamental reason for this lies mostly in the contrary requirements of responsivity and response speed for photocarrier lifetime.[16] Moreover, it is more challenging to maintain an outstanding optoelectronic performance under severe mechanical deformation, which seriously impedes the practical applications of flexible NIR-II photodetectors.

To address these issues, some effective strategies have been employed to simultaneously improve the optoelectronic performance and mechanical stabilities of flexible NIR-II photodetectors. One approach is to integrate commercial inorganic photodetectors with novel geometrical patterns and layouts such as a wavy structure, wrinkling patterns, mesh layouts, and so forth to dissipate the local strain on devices, realizing high optoelectronic performance under bending.[17−19] However, this strategy usually suffers from a complex fabrication process, limited wavelength detection, and low pixel resolution for monolithic integration of a highly responsive flexible photodetection system. Another strategy is to develop intrinsically flexible photosensing materials that simultaneously exhibit both high photosensitivity and mechanical stability. For example, inorganic nanomaterials and soft organic materials, such as two-dimensional materials,[6,20] colloidal quantum dots (QDs),[21−23] narrow-band

Received: December 13, 2022
Revised: February 15, 2023

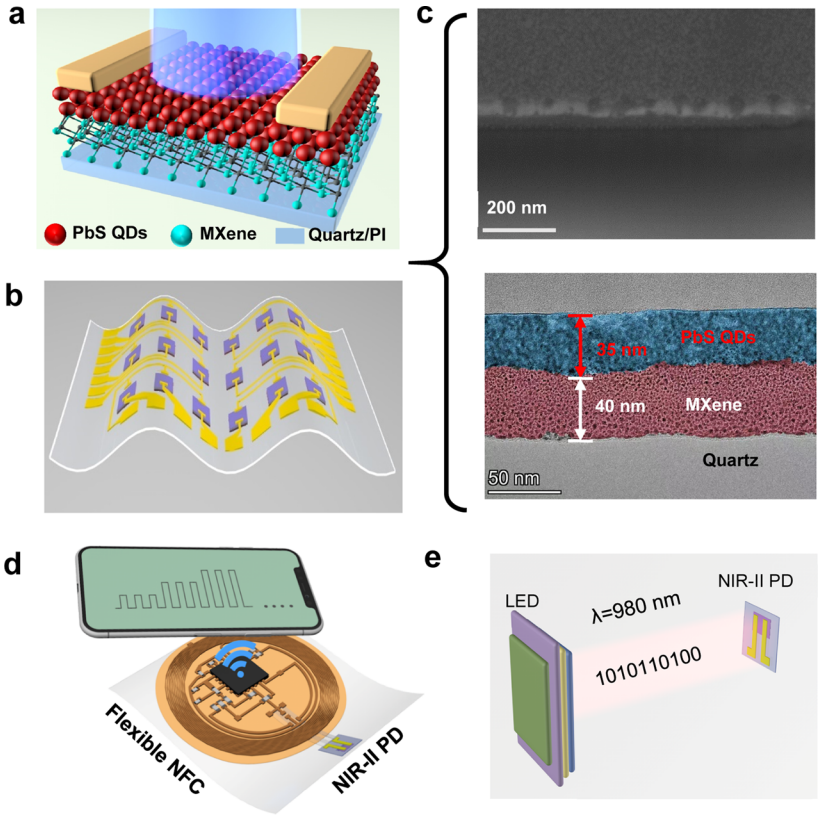

Figure 1. Materials synthesis and NIR-II photodetector fabrication. (a) Schematic of the MXene/PbS-based bilayer photodetector; (b) skin-like bilayer photodetector array prepared on a PI substrate; (c) cross-sectional scanning electron microscopy and transmission electron microscopy images of the bilayer film composed of MXene/PbS QDs; (d) schematic of the wireless photodetection system with flexible NFC and NIR-II photodetector; and (e) schematic of the optical communication via NIR-II light.

polymers, and small molecules,[24−27] have been developed to prepare flexible NIR-II photodetectors and arrays, but they usually exhibit weak photosensitivity due to inferior light absorption, low mobility, and high photocarrier recombination of the photosensing layers. To overcome these limitations, particularly in terms of photosensitivity, hybrid materials-based devices like phototransistors have been widely employed to maximize optoelectronic performance,[28] which successfully enhance the responsivity and detectivity by introducing traps to prolong the photocarrier lifetimes but usually sacrifice photoresponse speed.[15,29−32] Consequently, the possibilities of these phototransistors for practical applications in flexible and wearable optoelectronic systems remain limited due to their slow photoresponse (100 ms to 10 s), high gate voltage (20−80 V), and complicated structure.[15,29−31]

Here, we reported a skin-like bilayer photodetector prepared by combining a highly conducting MXene and photosensing PbS QDs to achieve both remarkable optoelectronic and mechanical performance. In particular, by integrating MXene film with PbS QDs, it efficiently promotes photocarrier separation at the interface of bilayer films and fast transport in spatially separated layers, leading to great enhancement simultaneously in responsivity, detectivity, and photoresponse speed. Thus, the resulting devices exhibit a rather high responsivity of around 1000 mA W^{-1}, detectivity exceeding 10^{11} Jones, and a photoresponse time of around 30 ms, which is the fastest photoresponse of a flexible NIR-II photoconductor among all bilayer devices based on PbS QDs. Moreover, the ultrathin thickness of active bilayers together with the strong bonding force at the interface of the MXene and PbS QDs can keep the photocarrier separation in the vertical direction and transport in the horizon direction highly efficient, leading to high optoelectronic performance under serve deformation. Thus, the skin-like NIR-II photodetectors prepared on ultraflexible polyimide (PI) substrates show a high retention of 95% optoelectronic performance after bending 500 cycles. All these together allow this device to demonstrate high performance for a flexible optoelectronic system that can be seamlessly integrated with curved substrates and 3D geometries to accurately distinguish and acquire real-time extensive information such as optical communication, NIR-II imaging, and proximity sensing.

2. RESULTS AND DISCUSSION

The high-quality PbS QDs and MXene nanosheets with uniform sizes were synthesized according to previous reports with modifications (see the Experimental Section), which are monodispersed in octane and water, respectively (Figure S1a).[33,34] The bilayer photodetector and array (6 × 3) were fabricated by sequentially spin-coating the MXene and PbS QDs on quartz and a skin-like PI substrate (Figure 1a), following the silver (Ag) electrode deposition via thermal evaporation (Figure 1a,b). The resulting devices form a stacked MXene/PbS QDs bilayer film with a total thickness of less than 80 nm (Figure 1c). More details for the device and array fabrication and optimization are shown in the Supporting Information. Figure 1d,e demonstrates the application scenarios for a wireless and battery-free near field communication (NFC) system for proximity sensing and optical communication, as is discussed in detail below.

https://doi.org/10.1021/acs.chemmater.2c03701
Chem. Mater. XXXX, XXX, XXX−XXX

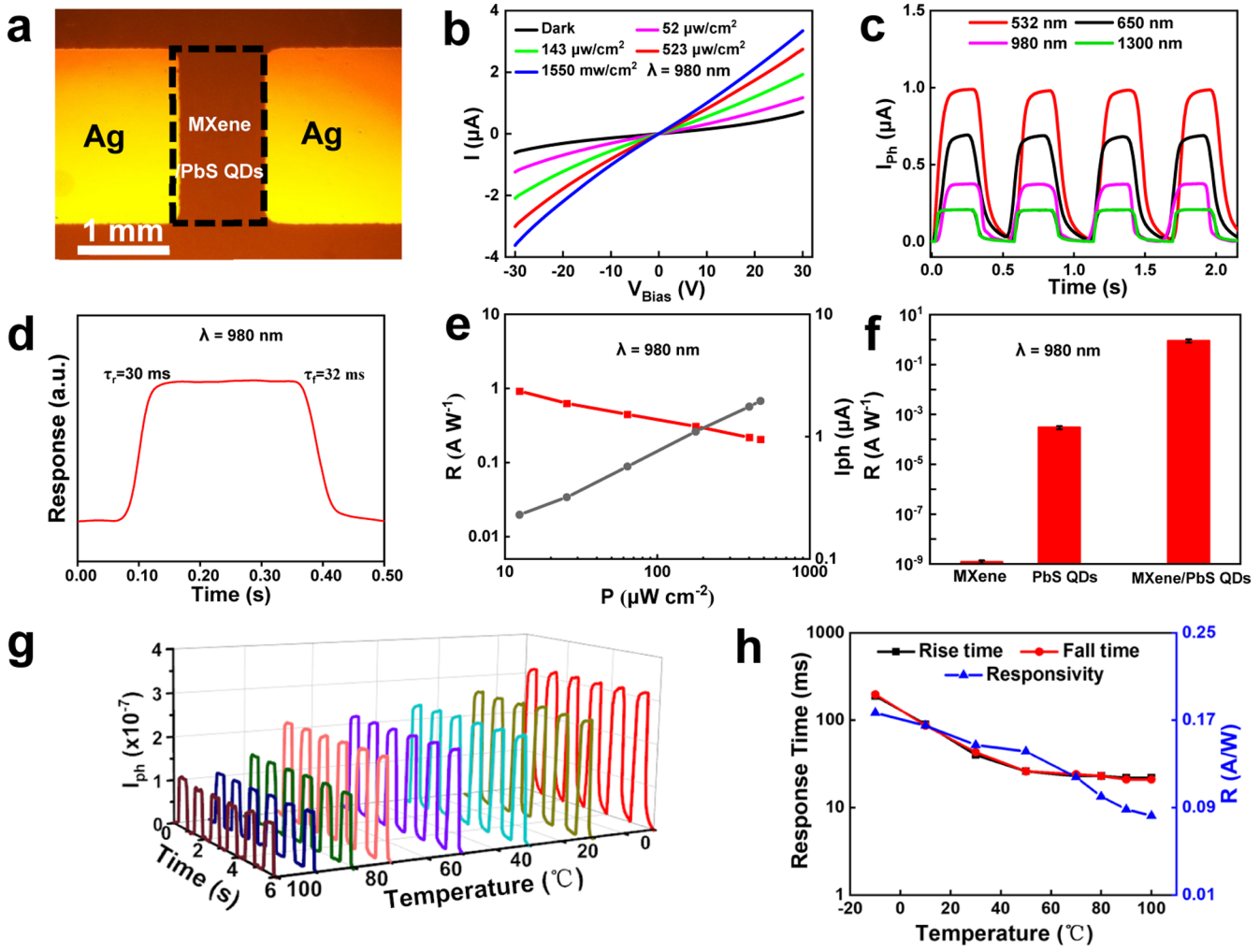

Figure 2. Evaluations of ultrathin NIR-II photodetectors. (a) Optical image of the MXene/PbS QDs-based bilayer photodetector on quartz ($L \times W$ = 1 mm × 2 mm); (b) I–V curves of the device in the dark and under light irradiation at a wavelength of 980 nm with various light intensities; (c) photoresponse of the device under irradiation at various wavelengths at 100 μW cm^{-2} at 2 Hz; (d) photoresponse and recovery time of the device under light irradiation at a wavelength of 980 nm; (e) photocurrent and responsivity of the device under different light intensities at 980 nm; (f) responsivities of the device prepared by pure MXene, PbS QDs, and MXene/PbS QDs at a wavelength of 980 nm with a light intensity of 20 μW cm^{-2}; (g) photocurrent of the device at various temperatures ranging from 0 to 100 °C under light irradiation with a wavelength of 980 nm; and (h) responsivity and response/recover time of the device at various temperatures.

To comprehensively evaluate the performance of NIR-II photodetectors and exploit their applications in flexible devices, we carefully optimized and measured the figures of merit of the device and compared with that of other bilayer NIR-II photodetectors. Here, a typical device was fabricated on a quartz substrate (Figure 2a), which shows almost linear voltage–current (I–V) curve in the dark, in a manner that is symmetric around 0 V, indicating a photoconductive character of the device that can work at broad bias (Figure 2b). Under light irradiation at 980 nm, the photocurrent at different irradiance values can be described as follows

$$\Delta I_{DS} = P_{light} \times \frac{\eta q \lambda}{hc} \times \frac{V\mu}{L^2} \times \tau \quad (1)$$

where μ is the carrier mobility, η is the absorption coefficient, and τ is the lifetime of photocarriers.[16] Accordingly, the photocurrent is mainly determined by the light absorption coefficient, mobility, and lifetime of photocarriers at constant light irradiation and bias. Therefore, the thicknesses of MXene and PbS QD films, playing key roles in mobility, light absorbing efficiency, and photocarrier lifetime, were optimized via controlling their solution concentrations with a defined spinning speed in the spinning process, which are obtained using 3 and 10 mg mL^{-1}, respectively (Figure S2 and Table S1). Here, we selectively measured the wavelength-dependent photoresponse of the device in the visible to NIR-II region, which all shows reproducible photoresponse at the light intensity of 100 μW cm^{-2} (Figures 2c and S3). In comparison, devices prepared by only the MXene and PbS QDs exhibit extremely weak photoresponse under irradiation due to their metallic properties and low mobility, respectively (Figures S4 and S5). It is worth mentioning that the bilayer device shows clear photoresponse to the spectrum of 1600 nm, which is beyond the absorption limit of PbS QDs (Figures S1e and S6). This unusual response is attributed to the existence of impurity levels in the PbS QD film that absorb the photons with low energy and get excited to the conduction band, which is enhanced by the MXene simultaneously.[32]

Response speed is a critical parameter of a photodetector, especially in real-time optical communication, imaging, and

https://doi.org/10.1021/acs.chemmater.2c03701
Chem. Mater. XXXX, XXX, XXX−XXX

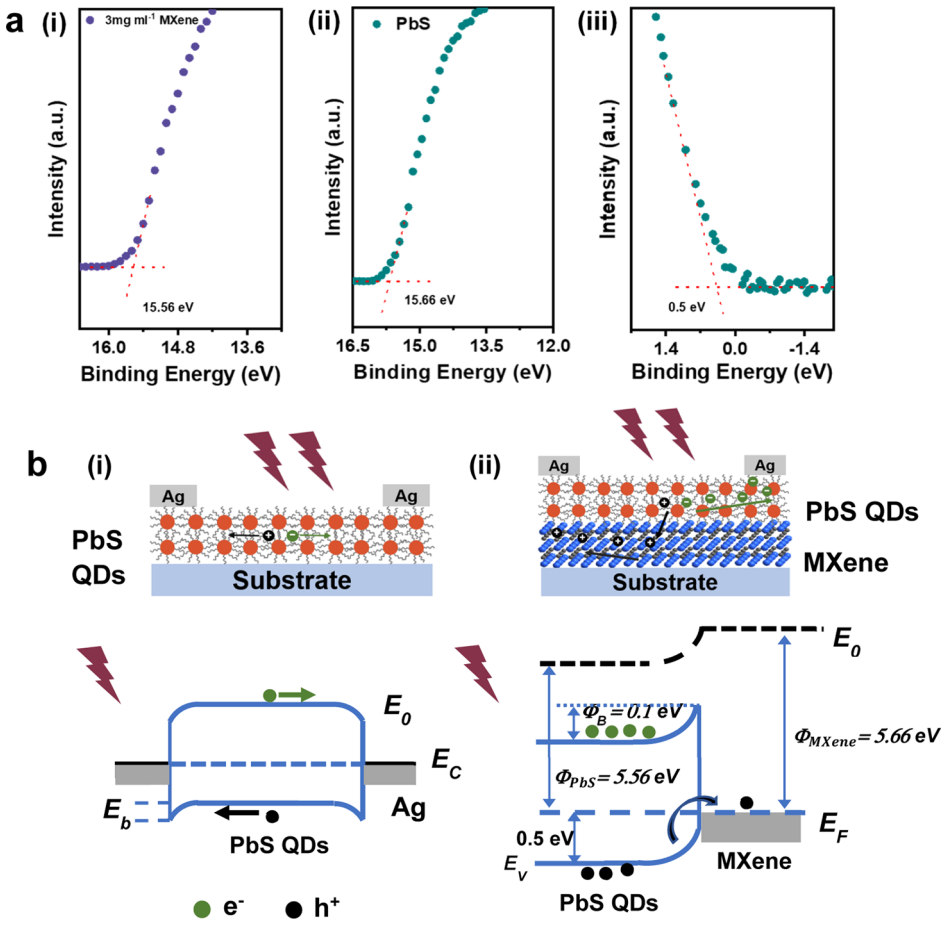

Figure 3. Working mechanism of NIR-II photodetectors. (a) UPS results of MXene (i) and PbS QDs (ii,iii) and (b) schematic and the corresponding band diagrams of the device made of PbS QDs (i) and MXene/PbS QDs (ii).

detection.[35,36] Here, we selectively measured the transient time by irradiating the device at the wavelength of 980 nm (Figure 2d) as an example. Remarkably, the device shows an extremely fast onset of the photocurrent under light irradiation and then reaches saturation with the same response and a recovery time of ~30 ms, which is the fastest NIR-II photodetector compared with other bilayer photoconductors based on PbS QDs so far, as shown in Table S2. This speedy photoresponse implies its great potential in the imaging applications, which typically require 30 frames per second. In most mixed-dimensional heterojunction-based phototransistors, the conducting channels are semiconductors, such as graphene,[30] molybdenum disulfide (MoS_2),[29] and carbon nanotubes,[31] which form high-density traps due to polar molecules absorptions, defects, and surface functional groups that prolong the lifetime of minor photocarriers, leading to high photoresponse but sacrificing the photoresponse speed. As noted previously, photodetectors are based on MXenes, where the MXene forms an ideal Schottky junction in the devices; thus, these devices exhibit superior performance in terms of photoresponse speed compared to the devices prepared by conventional metal electrodes without inducing excess traps.[37−39] Therefore, the MXene layer in our devices should have similar functions and a negligible influence on the lifetimes of photocarrier generated in PbS QDs. The efficient photocarrier separation at the interface of bilayers and the fast transport of photocarrier in MXene make our devices have a superior response and recovery speed.

Responsivity (R) and specific detectivity (D^*) are crucial figures of merit for assessing the sensitivity of the photodetector, in which R is defined as the ratio between the photocurrent (J_{photo}) and the light intensity (P_{light})

$$R = \frac{J_{photo}}{P_{light}} = \frac{\eta q \lambda}{hc}\frac{\tau}{\tau_T}, \tau_T = \frac{L^2}{V\mu} \quad (2)$$

where η is the absorption efficiency, τ is the trap lifetime, τ_T is the majority carrier transit time, h is the Plank's constant, q is the elementary charge, c is the light speed, L is the channel length, V is the applied bias, and u is the carrier mobility.[16] Figure 2e displays the dependence of the photocurrent and responsivity on the incident power of light with the wavelength of 980 nm at the power range from 12.5 to 475.0 μW cm^{-2} with a linear relationship between the photocurrent and incident light power. The photoresponsivity of our device reaches ~1000 mA W^{-1} under light irradiation at a wavelength of 980 nm with an intensity of 18.4 μW cm^{-2}, higher than that of most of bilayer photodetectors or imagers at a similar region (Table S2). The decreasing photoresponsivity at higher light intensity is consistent with that in literature studies owing to traps existing in PbS QDs and at the interface of bilayer films.[40] Compared with devices made of only MXene (Figure S4) and PbS QDs films (Figure S5), the bilayer architecture, synergizing advantages of these two materials, including a high molar absorption efficient of PbS QDs (≈10^6 M^{-1} cm^{-1}) and a high conductivity of MXene (~10^3 S cm^{-1}),[14,41] enables

https://doi.org/10.1021/acs.chemmater.2c03701
Chem. Mater. XXXX, XXX, XXX−XXX

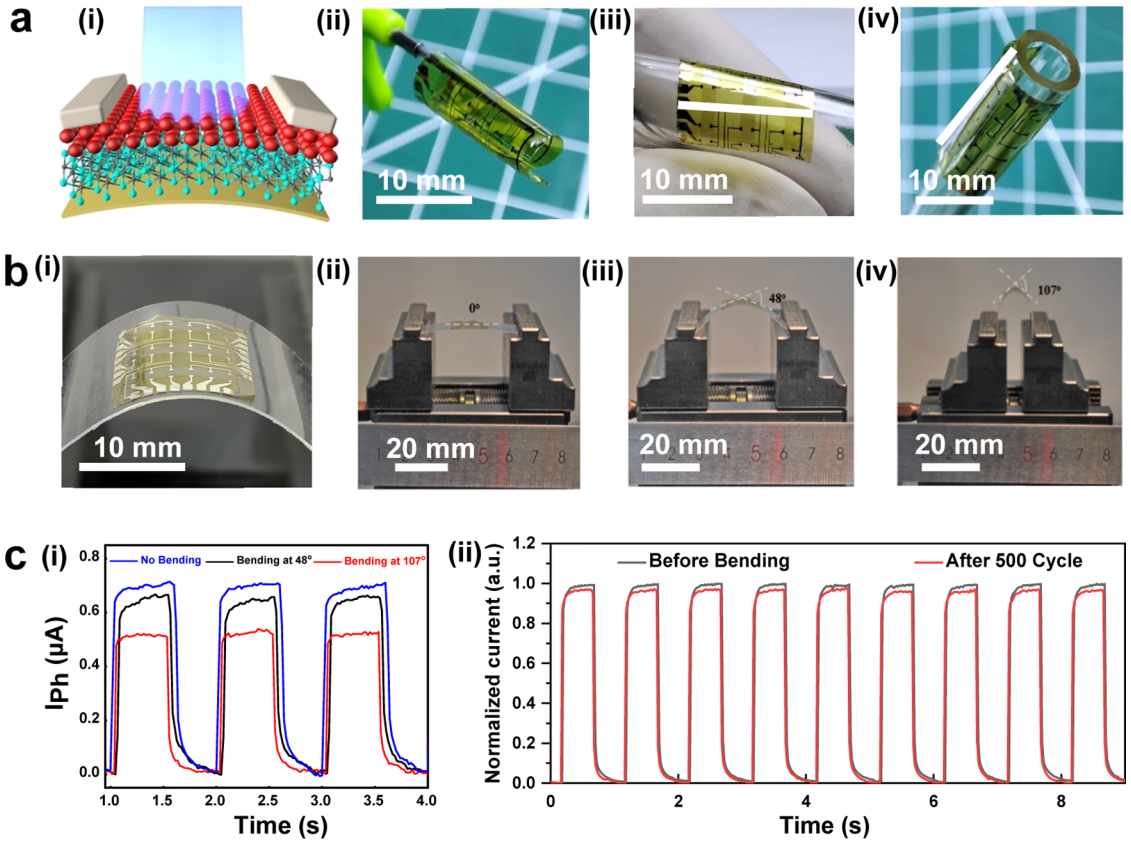

Figure 4. Flexibility evaluation of the skin-like NIR-II photodetector. (a) Schematic of an ultraflexible device on a PI substrate (i), needle (ii), PDMS (iii), and inside of the tube (iv); (b) photographs of devices attached on the PET substrate (i) and bending at different angles (ii–iv); (c) $I-T$ curves of the device at different bending angles under 980 nm illumination with a light intensity of 50 μW cm^{-2} at a bias voltage of 5 V (i), and photoresponse of flexible devices before and after bending for 500 cycles (ii).

photogenerated charges to be spatially separated and efficiently transferred to the MXene, which dramatically reduces carrier recombination and enhances the photocurrent. Consequently, the bilayer device shows extremely high photoresponsivity, which is 9 and 3 orders of magnitude higher than that of the MXene and PbS QDs-based devices, respectively (Figure 2f) at 980 nm. Note that our devices also demonstrate high photoresponsivity across the entire range from the visible region to NIR II region (Figures 2e and S2), for example, the photoresponsivity reaches over 1400 mA W^{-1} at 450 nm. The specific detectivity (D^*) is defined as follows

$$D^* = \frac{R\sqrt{A}}{\sqrt{2ei_{\text{dark}}}} \tag{3}$$

where i_{dark} is the dark current, A is the active area of the device, and e is the absolute value of the electronic charge (1.6×10^{-19} C).[42] The corresponding detectivity of our bilayer device under various light intensities is shown in Figure S7, which reaches over 10^{11} Jones (1 Jones = 1 cm Hz$^{1/2}$ W^{-1}). Equivalent power (NEP) is another critical parameter to quantify the limit of light power detection for a photodetector, which is defined as the minimum amount of light that can be detected at a signal-to-noise ratio of 1 for a 1Hz integration bandwidth and is described as follows

$$\text{NEP} = \frac{I_n}{R} \tag{4}$$

where I_n is the noise mainly generated by the high dark current in our photodetector. For the 980 nm illumination with the light intensity of 12 μW cm^{-2}, the NEP of our photodetector reaches as low as 0.125 nW.

To further explore the applications of the flexible NIR-II photodetector under different environmental conditions, here, we have investigated the optoelectronic performance of the device at elevated temperatures from 0 to 100 °C. As shown in Figure 2g, the device exhibits high reproducibility at 980 nm (at 50 μW cm^{-2}) and a clear photocurrent, and responses increase with the decrease of temperature from 100 to 0 °C (Figure 2h). The excellent response is attributed to the decrease of photon scattering and the increase of the lifetime of photocarriers in the bilayer device at low temperature.[43] To further validate this hypothesis, we examined the photoresponse and recovery time of the device at various temperatures, as summarized in Figure 2h. The response time decreases from 26 ms at 0 °C to 20 ms at 100 °C, and the corresponding recovery time decreases from 25 to 21 ms, indicating the short lifetime of photocarriers.

In order to gain insights into the working mechanism underlying the observed remarkable photoresponse, we first measured the working function of the MXene and PbS QDs by ultraviolet photoelectron spectroscopy (UPS), as shown in Figure 3a(i–iii). The working function of the MXene was determined to be approximately −5.66 eV with a zero band gap, which agrees well with previous reports.[37,38,44] In the case of PbS QDs, the Fermi level is calculated to be −5.56 eV with a band gap of 1.16 eV, and the valence band is 0.5 eV below

https://doi.org/10.1021/acs.chemmater.2c03701
Chem. Mater. XXXX, XXX, XXX−XXX

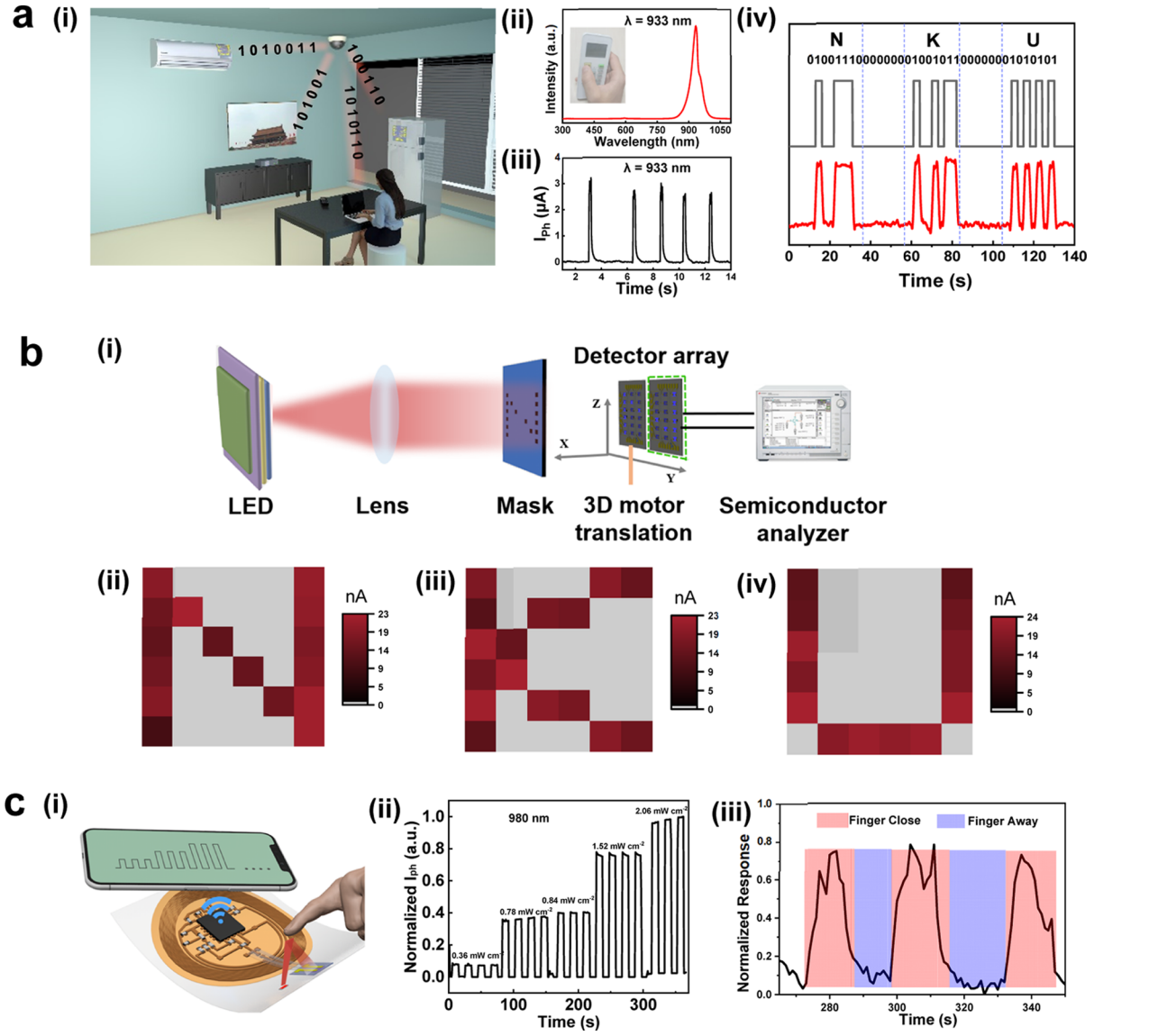

Figure 5. Applications of the skin-like NIR-II photodetector: optical communication, NIR-II imaging, and proximity sensing. (a) Schematic illustration of NIR communication utilized in an indoor environment (i), spectrum of NIR-II light used in an air conditioner remote controller (ii) and the corresponding photoresponse of the NIR-II photodetector under the irradiation of a remote controller (iii), and message code generated by an LED and the corresponding photoresponse of the photodetector (iv); (b) symbolic schematics for the imaging system employing a bilayer photodetector array as a photodetector (i) and the imaging result of "N", "K", and "U" letters (ii–iv); and (c) schematic of the proximity sensing system with a combination of a flexible NFC system, a mobile phone, an NIR-II photodetector, and an NIR-II LED (i), normalized photoresponse of the photodetector integrating with an NFC system at various light intensities (ii), and time-dependent photoresponse of the bilayer photodetector depending on the hand position (iii).

the Fermi level. To describe the photocurrent generation and transport in the PbS QDs film and MXene/PbS QDs-based photodetector, the band diagram and working mechanisms of the device are shown in Figure 3b.

For the device only composed of PbS QDs with a long channel length [Figure 3b(i)], the photoexcited carriers are separated and drift in the single-layer PbS QD film under external bias, which have considerable chances to recombine due to low mobility and long transport length, resulting in weak photoresponse [Figures 3b(i) and S4]. According to the Schottky–Mott rule related to the contact between the metal and semiconductor, the barrier between Ag and PbS QDs is high according to the band alignment, which further hinders the collection of photocarriers [Figure 3b(i)].[45] In the case of a bilayer device shown in Figure 3b(ii), the difference of work functions of MXene and PbS QDs drive electrons from PbS QDs to MXene, forming a Schottky junction at the interface of bilayer films. Under light irradiation, the photoabsorption in PbS QDs generates electron–hole pairs, which are separated at the MXene/PbS QDs interface due to the built-in electric field caused by the work function mismatch between PbS QDs and MXene.[44] As there is a large number of traps existing in PbS QDs and the interface of bilayers caused by defects, ligands, and surface groups, photogenerated electrons are more likely to be captured, which prolong the lifetime of electrons.[29−31] Moreover, photogenerated holes are more easily to transfer from PbS QDs to MXene films due to the built-in electric field pointing from PbS QDs to MXene, which can enable fast transit across the device due to the high conductivity of the MXene. Compared to the single-layer PbS QDs-based device

https://doi.org/10.1021/acs.chemmater.2c03701
Chem. Mater. XXXX, XXX, XXX−XXX

(Figure S5), the bilayer devices exhibit superior performance in terms of photosensitivity and response speed for a few reasons. First, the photocarriers generated in PbS QDs are transported in spatially separated layers, largely reducing the recombination chances. In addition, the difference of lifetimes of photogenerated electrons and holes in the bilayer device causes a photoconductive gain and improves the photoresponsivity.[44] Finally, ligands wrapped on PbS QDs also play vital roles in photoresponsivity. Here, we selected mercaptoacetic acid (MPA) as a ligand to treat PbS QDs due to its short length and hydrophilic carboxyl groups, which can form an interfacial interaction with MXene terminated with fluoride (−F), oxygen (−O), and hydroxyl (−OH) by secondary bond force, further leading to efficient photocarrier separation.[38,39] To validate this hypothesis, we also fabricated the bilayer devices using PbS QDs wrapped by long-length or hydrophobic ligands, including hexadecyl trimethyl ammonium bromide (CTAB), tetrabutylammonium iodide (TBAI), and ethanedithiol (EDT), and found that the devices exhibit poor optoelectronic performance (Figure S8 and Table S1) due to their weak interaction between PbS QDs and the MXene and inefficient photocarrier separation and transport. Unlike the previously reported devices that improved photoresponsivity by prolonging photocarriers lifetime via a photogating effect,[15,29−32] the MXene film shows high conductivity with a stable work function, which can promote the photocarrier transport without inducing traps, leading to fast photoresponse. In addition, Ag instead of the MXene and PbS QDs as bilayers does not produce obvious light response (shown in Figure S9).

Benefiting from the flexibility of the PI substrate and MXene/PbS QDs bilayer thin film, the skin-like photodetector array was fabricated on the PI substrate with a total thickness of less than 15 μm [Figure 4a(i,ii)]. The obtained skin-like device well conforms to various substrates including soft polydimethylsiloxane (PDMS), a 3D plastic tube with an inner diameter of less than 3 mm [Figure 4a(iii,iv)], and a flexible polyethylene terephthalate (PET) film under bending [Figure 4b(i)]. Figure 4b(ii−iv) displays the photograph of flexible devices attached on a PET film with different bending angles from 0 to 107°. Figure 4c(i) presents the $I-T$ curves of the flexible devices under light irradiation with a wavelength of 980 nm bending at different angles, which shows a negligible change in the dark current, indicating that the bending strain can hardly affect the electric performance of the device. It is clearly seen that the photocurrent slightly decreases with the increase of bending angles, which is due to the change of light intensity as the device deviated from the optical focus of NIR-II light. This hypothesis is further supported by the durability test for the same device after bending 500 cycles, which show a high retention of 95%, indicating the extremely high stability [Figures 4c(ii) and S10]. These results clearly demonstrate the excellent optoelectronic stability of this bilayer NIR-II skin-like photodetector under severe mechanical deformation. We ascribe this remarkable performance to the synergistic effect of the superior advantages of materials, ultrathin thickness, and the bilayer configuration. To further improve the mechanical stability of the ultraflexible photodetector, an efficient route is to introduce a suitable ligand that well disperses PbS QDs and reacts with the functional groups on the MXene to form a solid interface, which could release the internal strain and decrease cracks under bending, leading to a high charge transfer efficiency and negligible performance degradation. The outstanding optoelectronic properties of the photosensing materials primarily ensure that the device exhibits high sensitivity and fast photoresponse with ultrathin thickness. Moreover, in the bilayer device, photocarriers generated in PbS QD films are efficiently separated at the interface of PbS QDs and MXene, where photocarriers are transported across the spatially separated layers, even under mechanical deformation. As discussed above, there exists a strong bonding force between ligands and functional groups on the MXene at the interface of bilayers, which forms a steady interface for photocarrier separation and transport. All these factors above ensure that the device exhibits excellent optoelectronic performance and outstanding deformation tolerance.

We have confirmed that our skin-like NIR-II photodetector exhibits both excellent optoelectronic and mechanical performances. To verify this excellent performance in real-world applications, here, we fabricated some prototypes of flexible devices and systems to exploit their applications in NIR-II communication, imaging, and proximity sensing. NIR optical communication plays an important role in soft robotics, internet of things (IOT), and human−computer interaction that achieve communication between a machine and a human [Figure 5a(i)]. To evaluate the potential of NIR photodetectors in the optical communication, we applied our device in the air conditioner remote control. It is seen that the spectrum of the remote controller centers at 933 nm with a half-band width of 50 nm, which is within the photoresponse of the bilayer photodetector [Figure 5a(ii)]. The device shows a sharp increase in the photocurrent under the controller light irradiation and then drops to the initial state when the light is off [Figure 5a(iii)]. Moreover, we also encoded the information by the American Standard Code for Information Interchange (ASCII) using NIR-II light. During the light communication, the codes of letters “N”, “K”, and “U” were generated by the light-emitting diode (LED) with a wavelength of 980 nm driven by a signal generator [Figure 5a(iv)]. By integrating the NIR-II light with a photodetector on the consumer devices including an air conditioner, a television, and a refrigerator, it is possible to control these devices via an NIR-II LED assembled on a mobile phone for potential applications in the IOT.

NIR imaging also plays crucial roles in biomedical, military, and civil fields, especially in the future light-weight NIR imaging system that requires a high-resolution and light-weight NIR photodetector. Here, we designed and fabricated skin-like photodetector arrays (6 × 3), which were integrated with the LED (980 nm wavelength), lens, and shadow masks with letters “N”, “K”, and “U” [Figure 5b(i)]. The image is obtained by transforming the photocurrent obtained in each pixel into a green code, which is shown in Figure 5b(ii−iv). As the skin-like NIR-II photodetector can be solution processed into high-resolution imagers via appreciate design, it shows huge potential applications in the future low-cost and light-weight night vision and wearable optoelectronic systems.

The LiDAR system equipped with the NIR-II photodetector is widely used in the modern autopilot system for position detection due to its superior advantages compared to other spectra.[1] Therefore, a high-performance NIR-II photodetector is the key requirement of the system for imaging and distance measurement. Here, we prepared a prototype of a flexible proximity sensing system for position measurement [Figure 5c(i)] by integrating a skin-like NIR-II photodetector with a battery-free NFC wireless system (Figures S1 and S12) working in 13.6 MHz (Figure S14). The NFC system can

https://doi.org/10.1021/acs.chemmater.2c03701
Chem. Mater. XXXX, XXX, XXX−XXX

store and wirelessly send information containing distance through NIR-II light reflected from a finger or other objects.[46] The wireless proximity sensor shows fast and reproducible photoresponse to NIR-II light with a wavelength of 980 nm at different irradiance values [Figure 5c(ii)], which is in consistent with the wired photodetector. When the finger is closer to the sensor, more light will be reflected on the sensor and generate a higher photocurrent, as shown in Figure 5c(iii), while the current drops when the hand is away due to less light irradiated on the sensor.

3. CONCLUSIONS

We fabricated a high-performance, skin-like NIR-II photodetector and arrays that combined a highly conducting MXene and photosensitive PbS QDs with a bilayer structure. The synergistic effect of highly photosensitive materials as well as the bilayer configuration enables the device to exhibit a high photoresponsivity of around 1000 mA W^{-1}, a high detectivity of 10^{11} Jones, a low NEP of 0.125 nW, and a fast photoresponse time of 30 ms in the NIR-II spectrum. Owing to the high-performance photosensing materials, ultrathin thickness, and bilayer configuration, the device retains above 95% of optoelectronic performance after bending 500 cycles. In addition, the bilayer NIR-II photodetector shows remarkable optoelectronic performance at various temperatures from 0 to 100 °C, implying its potential applications in various environmental conditions. Moreover, the ultrathin feature of the skin-like NIR-II photodetector allows it to be wrapped on curved substrates and 3D geometries to accurately distinguish and acquire real-time extensive information. As example applications where NIR-II photodetectors can be applied in information and sensing technology, here, we show that our skin-like NIR-II photodetector can be well-integrated with the modern flexible wireless platforms used in optical communication, NIR-II imaging, and proximity sensing. This high-performance skin-like NIR-II photodetector can be highly beneficial to the next-generation optoelectronic devices, especially in skin electronics such as the light-weight night-vision system, biological imaging, optical communication, and artificial vision system used in soft robotics.

4. EXPERIMENTAL SECTION

4.1. Materials. The MXene was synthesized according to the previously reported protocols.[33] LiF (1 g, Sigma-Aldrich) was dissolved in the solution containing 20 mL of distilled (DI) water and 6 mL of 12 M hydrochloric acid (HCl) (Sigma-Aldrich) followed by slowly immersing MAX (1 g, Ti_3AlC_2 purchased from 11 Technology Co., Ltd) powder into the acid solution. The resulting solution was then stirred with a magnetic stir bar at 35 °C for 24 h. Following the acid treatment, the mixture was washed 10 times with DI water via a centrifugation and decantation process (3500 rpm for 5 min for each time), until a pH of ∼ 6 was reached. After removing the supernatant solution, the multilayer MXene was obtained. To obtain single-layer or few-layer MXene nanosheets, the multilayer MXene was dispersed in DI water, sonicated in an ice water bath for 1 h, and subsequently centrifuged at 3500 rpm for 60 min to collect the upper suspension. The resulting MXene solution was diluted by DI water to obtain the MXene solution with desired concentration.

The synthesis of PbS QDs was carried out following a previous report via the hot injection method.[47] PbO (0.223 g, 1 mmol) was dissolved in 0.64 mL of oleic acid and 2.0 mL of octadecene (ODE) in a three-necked flask, and the mixture is magnetically stirred at 35 °C under vacuum for 6 h, subsequently filling argon to remove moisture. Then, the mixture was heated up to 90 °C and kept for 3 h, and the mixture transforms into transparent liquid. The mixture was further heated to 120 °C, followed by loading bis(trimethylsilyl) sulfide (70 μL) to terminate the reaction. Thereafter, the oil heater was turned off and the flask stayed in the oil until it naturally cooled down to room temperature. To obtain the desired PbS QDs, the QDs were redispersed by acetone and separated by a centrifugation process at 5000 rpm for 20 min. This process was repeated a few times until there was no solid PbO suspending in acetone. The obtained PbS QDs were dried at 120 °C in the vacuum for 12 h and redispersed in octane with a concentration of 10 mg mL^{-1}.

4.2. Device Fabrication. The glass substrates were washed with soap, DI water, ethanol, and acetone and subsequently treated by ozone for 15 min. MXene solutions with different concentrations (1, 2, 3, and 4 mg mL^{-1}) were spin-coated on glass with the speed of 800 rpm for 30 s and then with the speed of up to 2000 rpm for 60 s to obtain a uniform film. The PbS QD octane solution (10 mg mL^{-1}) was subsequently spin coated on MXene film with the speed of 2500 rpm for 30 s. The spinning process of PbS QDs was repeated three times to get a ∼40 nm PbS film. Furthermore, the ligand methanol solution, including MPA, CTAB, TBAI, and EDT, was spin-coated on PbS QD film to remove the oleic ligand at a speed of 3000 rpm for 30 s. Finally, a 100 nm Ag film was deposited on the PbS film using a predesigned mask through the thermal evaporation technique. For the skin-like NIR-II photodetector, the PI precursor (Sigma-Aldrich) was spin-coated on cleaned glass with the speed of 3000 rpm for 1 min, followed by baking at 250 °C for 1 h. The obtained PI film was treated by UV ozone for 20 min, and then, devices were prepared following the process of the rigid device. The process of design and fabrication of the NFC wireless patch follows our previous report,[46] in which the Cu/PI film (Pyralux AC182000R) was patterned by standard photolithography via a predesigned photomask. The resistors, capacitors, and NFC chips were bonded on the patch using solder paste. The data of wireless system were read from the ADC ports that can be accessed using GUI software from Texas Instrument.

4.3. Materials and Devices Characterizations. The UV−vis spectrometric absorption of MXene and PbS QD solutions and films were measured using a UV−vis spectrometer (Cary 3000). The thickness and morphology of single MXene nanosheets were characterized using atomic force microscopy (Bruke Multimode 8). X-ray diffraction of PbS QDs and MXene were obtained by a Rigaku III (Cu Kα λ = 0.154 nm). The UPS analysis was performed on a Thermo Fisher ESCALAB 250Xi (He I 21.22 eV), and cross-section images of MXene and PbS QDs were obtained by focused ion beam transmission electron microscopy (TESCAN Solaris, FEI Talos F200XG2 AEMC). To examine the optoelectronic performance of the device, current−voltage (I−V) and current−time (I−T) curves in the dark and under irradiation were tested by a semiconductor parameter analyzer (Keysight B1500A) combined with lasers of different wavelengths (Oxlaser) and Chopper (RS540 Chopper Controller, Stanford Research System. Inc). The photoresponse and recovery time of the device was measured by an oscilloscope (MDO4104C, Tektronix) equipped with a laser (Oxlaser) driven by a signal generator (DG992, RIGOL).

4.4. Imaging, Proximity Sensing, and Optical Communication. For the optical communication, the NIR-II light installed on the remote controller of an air conditioner [Midea KFR-26GW/BP2DN8Y-DH400 (3)] works as a light source, which is irradiated on an NIR photodetector for information transfer. The spectrum of light on the remote controller is characterized by a spectrometer (Ocean Optics USB 4000). To achieve optical communication via an ASCII code, the information was encoded by emitting NIR light via an LED controlled by a signal generator. Particularly, the logical "0" and "1" represent the command "off" and "on" of the NIR light, respectively, which can be received by the NIR-II photodetector and generate photocurrent to response message. Here, letters of "N", "K", and "U" are corresponding to ASCII values of "01001110", "01001011", and "01010101", respectively. Visible and NIR imaging of the photodetector array is carried out by measuring the photocurrent of the device under pulse light generated by an LED. Hollow masks with letters of "N", "K", and "U" were installed between

https://doi.org/10.1021/acs.chemmater.2c03701
Chem. Mater. XXXX, XXX, XXX−XXX

the lens and photodetector array to generate images. The photocurrents of photodetectors under light irradiation were collected by a source meter (Keithley 2400 Source Meter Controlled by the Software developed by Wuhan Zeal Young Technology Co., Ltd.). Here, we chose green light (520 nm) and NIR-II light (980 nm) as the light source to assess the imaging capability of the photodetector array (Figure S15). The photodetector was integrated with an NFC wireless system and was encapsulated by a thin PDMS film (detail in Note S1), which can be attached on the arm or other substrates. An NIR-II LED with a wavelength of 850 nm (Huashang HSE850-L504) was attached on the PDMS film close to the photodetector. When the finger is close to the photodetector, the current of the system increases due to the reflection of NIR light on the photodetector, while the current decreases when the finger is away.

■ ASSOCIATED CONTENT

Supporting Information

The Supporting Information is available free of charge at https://pubs.acs.org/doi/10.1021/acs.chemmater.2c03701.

Additional experimental details on device fabrication and material characterizations; optoelectronic performance characterizations of single-layer and bi-layer devices; mechanical performance characterizations of flexible devices; NFC wireless system design, fabrication, and characterizations; setup of the imaging system for photodetectors; comparison of optoelectronic performance of devices treated by different ligands; table and comparison of optoelectronic performance of bilayer devices prepared with PbS QDs; components of the NFC wireless system; working mechanism of the NFC system and proximity system (PDF)

■ AUTHOR INFORMATION

Corresponding Authors

Guanghui Li − *The Centre of Nanoscale Science and Technology and Key Laboratory of Functional Polymer Materials, Institute of Polymer Chemistry, Renewable Energy Conversion and Storage Center (RECAST), College of Chemistry, Nankai University, Tianjin 300071, China*; Email: ghli1127@nankai.edu.cn

Yongsheng Chen − *The Centre of Nanoscale Science and Technology and Key Laboratory of Functional Polymer Materials, Institute of Polymer Chemistry, Renewable Energy Conversion and Storage Center (RECAST), College of Chemistry, Nankai University, Tianjin 300071, China; State Key Laboratory of Elemento-Organic Chemistry, Nankai University, Tianjin 300071, China*; orcid.org/0000-0003-1448-8177; Email: yschen99@nankai.edu.cn

Authors

Yu Zhu − *The Centre of Nanoscale Science and Technology and Key Laboratory of Functional Polymer Materials, Institute of Polymer Chemistry, Renewable Energy Conversion and Storage Center (RECAST), College of Chemistry, Nankai University, Tianjin 300071, China*

Chen Geng − *The Centre of Nanoscale Science and Technology and Key Laboratory of Functional Polymer Materials, Institute of Polymer Chemistry, Renewable Energy Conversion and Storage Center (RECAST), College of Chemistry, Nankai University, Tianjin 300071, China*

Lianghao Hu − *The Centre of Nanoscale Science and Technology and Key Laboratory of Functional Polymer Materials, Institute of Polymer Chemistry, Renewable Energy Conversion and Storage Center (RECAST), College of Chemistry, Nankai University, Tianjin 300071, China*

Lin Liu − *i-Lab, Key Laboratory of Multifunctional Nanomaterials and Smart Systems, Suzhou Institute of Nano-Tech and Nano-Bionics (SINANO), Chinese Academy of Sciences (CAS), Suzhou, Jiangsu 215123, China*

Yangzhi Zhu − *Terasaki Institute for Biomedical Innovation, Los Angeles, California 90064, United States*; orcid.org/0000-0003-2920-3365

Yao Yao − *Department of Aerospace Engineering, The Pennsylvania State University, University Park, Pennsylvania 16802, United States*

Chenxi Li − *The Centre of Nanoscale Science and Technology and Key Laboratory of Functional Polymer Materials, Institute of Polymer Chemistry, Renewable Energy Conversion and Storage Center (RECAST), College of Chemistry, Nankai University, Tianjin 300071, China*

Yanfeng Ma − *The Centre of Nanoscale Science and Technology and Key Laboratory of Functional Polymer Materials, Institute of Polymer Chemistry, Renewable Energy Conversion and Storage Center (RECAST), College of Chemistry, Nankai University, Tianjin 300071, China*

Complete contact information is available at: https://pubs.acs.org/10.1021/acs.chemmater.2c03701

Author Contributions

Y.C. and G.L. conceived and designed the project. Y.Z. fabricated the skin-like NIR-II photodetector and carried out all of the performance studies. The manuscript was mainly prepared by Y.C., G.L., Y.Z., and C.L., and all authors participated in the manuscript preparation and commented on the manuscript.

Funding

The financial support from NSFC (21935007) and MoST (2019YFA0705900) of China, Tianjin city (20JCZDJC00740), the 111 Project (B12015), the 100 Young Academic Leaders Program of Nankai University (020-ZB22000110 and 020-ZB22000110), and the Haihe Laboratory of Sustainable Chemical Transformations is acknowledged.

Notes

The authors declare no competing financial interest.

■ REFERENCES

(1) Hong, G.; Antaris, A. L.; Dai, H. J. Near-infrared fluorophores for biomedical imaging. *Nat. Biomed. Eng.* **2017**, *1*, 10.

(2) Park, S.; Heo, S. W.; Lee, W.; Inoue, D.; Jiang, Z.; Yu, K.; Jinno, H.; Hashizume, D.; Sekino, M.; Yokota, T.; Fukuda, K.; Tajima, K.; Someya, T. Self-powered ultra-flexible electronics via nano-grating-patterned organic photovoltaics. *Nature* **2018**, *561*, 516−521.

(3) Chow, P. C. Y.; Someya, T. Organic photodetectors for next-generation wearable electronics. *Adv. Mater.* **2020**, *32*, 1902045.

(4) Lee, G. H.; Moon, H.; Kim, H.; Lee, G. H.; Kwon, W.; Yoo, S.; Myung, D.; Yun, S. H.; Bao, Z.; Hahn, S. K. Multifunctional materials for implantable and wearable photonic healthcare devices. *Nat. Rev. Mater.* **2020**, *5*, 149−165.

(5) Kim, I.; Martins, R. J.; Jang, J.; Badloe, T.; Khadir, S.; Jung, H. Y.; Kim, H.; Kim, J.; Genevet, P.; Rho, J. Nanophotonics for light detection and ranging technology. *Nat. Nanotechnol.* **2021**, *16*, 508−524.

(6) Mueller, T.; Xia, F.; Avouris, P. Graphene photodetectors for high-speed optical communications. *Nat. Photonics* **2010**, *4*, 297−301.

(7) Yan, T.; Li, Z.; Cao, F.; Chen, J.; Wu, L.; Fang, X. An all-organic self-powered photodetector with ultraflexible dual-polarity output for biosignal detection. *Adv. Mater.* **2022**, *34*, 2201303.

(8) Kim, J.; Kwon, S. M.; Kang, Y. K.; Kim, Y. H.; Lee, M. J.; Han, K.; Facchetti, A.; Kim, M. G.; Park, S. K. A skin-like two-dimensionally pixelized full-color quantum dot photodetector. *Sci. Adv.* **2019**, *5*, No. eaax8801.
(9) Park, S.; Fukuda, K.; Wang, M.; Lee, C.; Yokota, T.; Jin, H.; Jinno, H.; Kimura, H.; Zalar, P.; Matsuhisa, N.; Umezu, S.; Bazan, G. C.; Someya, T. Ultraflexible near-Infrared organic photodetectors for conformal photoplethysmogram sensors. *Adv. Mater.* **2018**, *30*, 1802359.
(10) Kim, J. J.; Wang, Y.; Wang, H. Y.; Lee, S.; Yokota, T.; Someya, T. Skin electronics: next-generation device platform for virtual and augmented reality. *Adv. Electron. Mater.* **2021**, *31*, 2009602.
(11) Song, J. K.; Kim, J.; Yoon, J.; Koo, J. H.; Jung, H.; Kang, K.; Sunwoo, S. H.; Yoo, S.; Chang, H.; Jo, J.; Baek, W.; Lee, S.; Lee, M.; Kim, H. J.; Shin, M.; Yoo, Y. J.; Song, Y. M.; Hyeon, T.; Kim, D. H.; Son, D. Stretchable colour-sensitive quantum dot nanocomposites for shape-tunable multiplexed phototransistor arrays. *Nat. Nanotechnol.* **2022**, *17*, 849−856.
(12) Kim, Y. R.; Phan, T. L.; Cho, K. W.; Kang, W. T.; Kim, K.; Lee, Y. H.; Yu, W. J. Infrared proximity sensors based on photo-induced tunneling in van der waals Integration. *Adv. Electron. Mater.* **2021**, *31*, 2100966.
(13) Chen, W. J.; Ahn, S.; Balingit, M.; Wang, J. Y.; Lockett, M.; Vazquez-Mena, O. Near full light absorption and full charge collection in 1-micron thick quantum dot photodetector using intercalated graphene monolayer electrodes. *Nanoscale* **2020**, *12*, 4909−4915.
(14) Ren, Z. W.; Sun, J. K.; Li, H.; Mao, P.; Wei, Y. Z.; Zhong, X. H.; Hu, J. S.; Yang, S. Y.; Wang, J. Z. Bilayer PbS quantum dots for high-performance photodetectors. *Adv. Mater.* **2017**, *29*, 1702055.
(15) Sun, Z.; Liu, Z.; Li, J.; Tai, G.-a.; Lau, S.-P.; Yan, F. Infrared photodetectors based on CVD-grown graphene and PbS quantum dots with ultrahigh responsivity. *Adv. Mater.* **2012**, *24*, 5878−5883.
(16) Fang, H.; Hu, W. photogating in low dimensional photodetectors. *Adv. Sci.* **2017**, *4*, 1700323.
(17) Ko, H. C.; Stoykovich, M. P.; Song, J. Z.; Malyarchuk, V.; Choi, W. M.; Yu, C. J.; Geddes III, J. B.; Xiao, J. L.; Wang, S. D.; Huang, Y. G.; Rogers, J. A. A hemispherical electronic eye camera based on compressible silicon optoelectronics. *Nature* **2008**, *454*, 748−753.
(18) Zhang, K.; Jung, Y. H.; Mikael, S.; Seo, J. H.; Kim, M.; Mi, H. Y.; Zhou, H.; Xia, Z. Y.; Zhou, W. D.; Gong, S. Q.; Ma, Z. Q. Origami silicon optoelectronics for hemispherical electronic eye systems. *Nat. Commun.* **2017**, *8*, 1782.
(19) Rao, Z. Y.; Lu, Y. T.; Li, Z. W.; Sim, Y. S.; Ma, Z. Q.; Xiao, J. L.; Yu, C. J. Curvy, shape-adaptive imagers based on printed optoelectronic pixels with a kirigami design. *Nat. Electron.* **2021**, *4*, 513−521.
(20) Youngblood, N.; Chen, C.; Koester, S. J.; Li, M. Waveguide-integrated black phosphorus photodetector with high responsivity and low dark current. *Nat. Photonics* **2015**, *9*, 247−252.
(21) Konstantatos, G.; Howard, I.; Fischer, A.; Hoogland, S.; Clifford, J.; Klem, E.; Levina, L.; Sargent, E. H. Ultrasensitive solution-cast quantum dot photodetectors. *Nature* **2006**, *442*, 180−183.
(22) McDonald, S. A.; Konstantatos, G.; Zhang, S. G.; Cyr, P. W.; Klem, E. J. D.; Levina, L.; Sargent, E. H. Solution-processed PbS quantum dot infrared photodetectors and photovoltaics. *Nat. Mater.* **2005**, *4*, 138−142.
(23) Liu, J.; Liu, P. L.; Chen, D. Y.; Shi, T. L.; Qu, X. X.; Chen, L.; Wu, T.; Ke, J. P.; Xiong, K.; Li, M. Y.; Song, H. S.; Wei, W.; Cao, J. K.; Zhang, J. B.; Gao, L.; Tang, J. A near-infrared colloidal quantum dot imager with monolithically integrated readout circuitry. *Nat. Electron.* **2022**, *5*, 443−451.
(24) Gong, X.; Tong, M. H.; Xia, Y. J.; Cai, W. Z.; Moon, J. S.; Cao, Y.; Yu, G.; Shieh, C. L.; Nilsson, B.; Heeger, A. J. High-detectivity polymer photodetectors with spectral response from 300 nm to 1450 nm. *Science* **2009**, *325*, 1665−1667.
(25) Lee, J.; Ko, S. J.; Lee, H.; Huang, J. F.; Zhu, Z. Y.; Seifrid, M.; Vollbrecht, J.; Brus, V. V.; Karki, A.; Wang, H. B.; Cho, K.; Nguyen, T. Q.; Bazan, G. C. Side-chain engineering of nonfullerene acceptors for near-Infrared organic photodetectors and photovoltaics. *ACS Energy Lett.* **2019**, *4*, 1401−1409.
(26) Li, W.; Xu, Y. L.; Meng, X. Y.; Xiao, Z.; Li, R. M.; Jiang, L.; Cui, L. H.; Zheng, M. J.; Liu, C.; Ding, L. M.; Lin, Q. Q. Visible to near-infrared photodetection based on ternary organic heterojunctions. *Adv. Funct. Mater.* **2019**, *29*, 1808948.
(27) Chen, Y. J.; Zheng, Y. Q.; Jiang, Y. Y.; Fan, H. J.; Zhu, X. Z. Carbon-Bridged 1,2-Bis(2-thienyl)ethylene: An extremely electron rich dithiophene building block enabling electron acceptors with absorption above 1000 nm for highly sensitive NIR photodetectors. *J. Am. Chem. Soc.* **2021**, *143*, 4281−4289.
(28) Cai, S.; Xu, X. J.; Yang, W.; Chen, J. X.; Fang, X. S. Materials and designs for wearable photodetectors. *Adv. Mater.* **2019**, *31*, 1808138.
(29) Kufer, D.; Nikitskiy, I.; Lasanta, T.; Navickaite, G.; Koppens, F. H. L.; Konstantatos, G. Hybrid 2D-0D MoS2-PbS quantum dot photodetectors. *Adv. Mater.* **2015**, *27*, 176−180.
(30) Konstantatos, G.; Badioli, M.; Gaudreau, L.; Osmond, J.; Bernechea, M.; de Arquer, F. P.; Gatti, F.; Koppens, F. H. L. Hybrid graphene-quantum dot phototransistors with ultrahigh gain. *Nat. Nanotechnol.* **2012**, *7*, 363−368.
(31) Park, S.; Kim, S. J.; Nam, J. H.; Pitner, G.; Lee, T. H.; Ayzner, A. L.; Wang, H. L.; Fong, S. W.; Vosgueritchian, M.; Park, Y. J.; Brongersma, M. L.; Bao, Z. A. Significant enhancement of infrared photodetector sensitivity using a semiconducting single-walled carbon nanotube/C60 phototransistor. *Adv. Mater.* **2015**, *27*, 759−765.
(32) Pradhan, B.; Das, S.; Li, J. X.; Chowdhury, F.; Cherusseri, J.; Pandey, D.; Dev, D.; Krishnaprasad, A.; Barrios, E.; Towers, A.; Gesquiere, A.; Tetard, L.; Roy, T.; Thomas, J. Ultrasensitive and ultrathin phototransistors and photonic synapses using perovskite quantum dots grown from graphene lattice. *Sci. Adv.* **2020**, *6*, No. eaay5225.
(33) Alhabeb, M.; Maleski, K.; Anasori, B.; Lelyukh, P.; Clark, L.; Sin, S.; Gogotsi, Y. Guidelines for synthesis and processing of two-dimensional titanium carbide ($Ti3C2T_X$ MXene). *Chem. Mater.* **2017**, *29*, 7633−7644.
(34) Hines, M. A.; Scholes, G. D. Colloidal PbS nanocrystals with size-tunable near-infrared emission: Observation of post-synthesis self-narrowing of the particle size distribution. *Adv. Mater.* **2003**, *15*, 1844−1849.
(35) Cao, F.; Yan, T.; Li, Z.; Wu, L.; Fang, X. Dual-band perovskite bulk heterojunction self-powered photodetector for encrypted communication and imaging. *Adv. Opt. Mater.* **2022**, *10*, 2200786.
(36) Cao, F.; Li, Z.; Liu, X.; Shi, Z.; Fang, X. Air induced formation of $Cs_3Bi_2Br_9/Cs_3BiBr_6$ bulk heterojunction and its dual-band photodetection abilities for light communication. *Adv. Funct. Mater.* **2022**, *32*, 2270263.
(37) Song, W.; Chen, J.; Li, Z.; Fang, X. Self-powered MXene/GaN van der waals heterojunction ultraviolet photodiodes with superhigh efficiency and stable current outputs. *Adv. Mater.* **2021**, *33*, 2101059.
(38) Kang, Z.; Ma, Y.; Tan, X.; Zhu, M.; Zheng, Z.; Liu, N.; Li, L.; Zou, Z.; Jiang, X.; Zhai, T.; Gao, Y. MXene-silicon van der waals heterostructures for high-speed self-driven photodetectors. *Adv. Electron. Mater.* **2017**, *3*, 1700165.
(39) Montazeri, K.; Currie, M.; Verger, L.; Dianat, P.; Barsoum, M. W.; Nabet, B. Beyond gold: spin-coated Ti3C2-based MXene photodetectors. *Adv. Mater.* **2019**, *31*, 1903271.
(40) Zhao, Q. H.; Wang, W.; Carrascoso-Plana, F.; Jie, W. Q.; Wang, T.; Castellanos-Gomez, A.; Frisenda, R. The role of traps in the photocurrent generation mechanism in thin InSe photodetectors. *Mater. Horiz.* **2020**, *7*, 252−262.
(41) Dillon, A. D.; Ghidiu, M. J.; Krick, A. L.; Griggs, J.; May, S. J.; Gogotsi, Y.; Barsoum, M. W.; Fafarman, A. T. Highly conductive optical quality solution-processed films of 2D titanium carbide. *Adv. Funct. Mater.* **2016**, *26*, 4162−4168.
(42) Ge, Z.; Xu, N.; Zhu, Y.; Zhao, K.; Ma, Y. F.; Li, G. H.; Chen, Y. S. Visible to mid-infrared photodetection based on flexible 3D graphene/organic hybrid photodetector with ultrahigh responsivity at ambient conditions. *ACS Photonics* **2022**, *9*, 59−67.

https://doi.org/10.1021/acs.chemmater.2c03701
Chem. Mater. XXXX, XXX, XXX−XXX

(43) Lee, J. J.; Kim, J. D.; Razeghi, M. Room temperature operation of 8-12 μm InSbBi infrared photodetectors on GaAs substrates. *Appl. Phys. Lett.* **1998**, *73*, 602−604.
(44) Zhu, J.; Wang, H.; Ma, L.; Zou, G. Observation of ambipolar photoresponse from 2D MoS2/MXene heterostructure. *Nano Res.* **2021**, *14*, 3416−3422.
(45) Li, G. H.; Suja, M.; Chen, M. G.; Bekyarova, E.; Haddon, R. C.; Liu, J. L.; Itkis, M. E. Visible-blind UV photodetector based on single-walled carbon nanotube thin film/ZnO vertical heterostructures. *ACS Appl. Mater. Interfaces* **2017**, *9*, 37094−37104.
(46) Li, G. H.; Yao, Y.; Ashok, N.; Ning, X. Ultra-flexible visible-blind optoelectronics for wired and wireless UV sensing in harsh environments. *Adv. Mater. Tech.* **2021**, *6*, 2001125.
(47) Hou, B.; Cho, Y.; Kim, B. S.; Hong, J.; Park, J. B.; Ahn, S. J.; Sohn, J. I.; Cha, S.; Kim, J. M. Highly monodispersed PbS quantum dots for outstanding cascaded-junction solar cells. *ACS Energy Lett.* **2016**, *1*, 834−839.

https://doi.org/10.1021/acs.chemmater.2c03701
Chem. Mater. XXXX, XXX, XXX−XXX